Computational measurements of stress fields from digital images

Julien Réthoré

Computational measurements of stress fields from digital images

J. Réthoré
Research Institute in Civil and Mechanical Engineering(GeM)
Ecole Centrale de Nantes, Université de Nantes
UMR 6183 CNRS, 1 rue de la Noë, F-44 123 Nantes, France.

February 2, 2017

1 Introduction

Since the pioneering work of Lucas, Kanade and others [1], image registration or Digital Image Correlation (DIC) has been widely used and developed in many ways. For mechanical experimentalists, the purpose of DIC is to measure displacement fields by comparing digital images of the sample under two different deformation states. Sub-set based techniques are the most popular (see for example [2]) because they are the techniques implemented in commercial softwares. One should also mention the non-parametric formulation proposed by [3] that allows for measuring a displacement field pixel-wise. Compared to the conventional experimental methodology for constitutive behaviour analysis, that consists in performing uni-axial homogeneous stress/strain tests, DIC has the great advantage to provide for full displacement and strain fields. While this is useful to assess the quality of conventional tests, making good use of the rich data extracted from DIC measurements is still the purpose of many research works. One of the main issues is that the stress field in heterogeneous state configurations cannot be accessed without coupling measurements with numerical simulations.

Recently, Besnard *et al.*proposed a finite element (FE) formulation for DIC [4]. This considerably increases the potential of DIC as a strong coupling with FE simulations is established. For example, it is shown in [5] that both DIC and elastic balance of momentum can be solved at the same time. For the characterization of material constitutive relations, this opportunity to couple DIC measurements with FE simulation has been exploited to design robust identification techniques [6, 7]. By identification we mean here estimating the parameters of a presupposed constitutive model. In some cases, making explicit a constitutive model and formalizing a constitutive law turns out to be extremely difficult. This is case for example for ductile tearing as the stress/strain and triaxiality levels occurring at the tip of a crack cannot be reached in homogeneous stress/strain test configurations. At this point, the advantage of this framework (FE DIC combine with FE simulation) reveals also to be a weakness as it requires the constitutive relation to be explicit.

To circumvent the difficulty of formulating a constitutive relation, manifold learning or dimensionality reduction [8] are good candidates. The idea is to use data bases of admissible material states (at least stress and strain) points to extract manifold and then to perform multi-dimensional interpolation/regression for calculating internal forces in FE simulations. The data-driven computational mechanics framework recently proposed in [9] goes one step further. Instead of minimizing the energy under the constraint that the constitutive relation is satisfied, the authors propose in this work to minimize the distance between the computed material states and those fulfilled by a data base under the constraint of equilibrium. These non-parametric approaches of the mechanics of materials have a great potential to circumvent the limitations of parametric approaches concerning the formulation of the constitutive relationship. However, if the data base that is used is fulfilled with results from conventional experiments using homogeneous stress/strain configurations, these promising methodologies would suffer from the same limitations concerning intense and/or complex loadings.

Full-field measurements could be used on heterogeneous states configuration to enrich material state data bases with more complex configurations. However, as it has been mentioned above, the stress analysis of complex tests requires the coupling with FE simulations that need a constitutive model. This is disappointing to observe that these two advanced methods (one that extracts material data from experiments and the other that makes use of material state data to perform simulations) cannot help each other. At this point, one ends up with this key question:

Is it possible to measure non-elastic stress fields ?

It has not yet been possible. There exist some optical techniques like photo-elasticity, caustics, or more recently Diffraction Computed Tomography, that lead to elastic stress fields but non-elastic stress evaluation is out of their scope. The aim of this paper is a proposition that may answer this question. It is not claimed that stress may become observable but we propose herein to formulate DIC so that stress and strain fields can be directly estimated with no assumption on the constitutive relation. Plus, a supplementary information is obtained that can be interpreted as an internal variable field that measures the distance between the actual local constitutive equation and linear elasticity according to a given but arbitrary elastic tensor. The method will be referred to as Mechanical Image Correlation (MIC) as it allows to measure from digital images the local mechanical state of a material.

In the first Section, the principle of DIC and the analysis of noise sensitivity are briefly explained. Then, the details of MIC are provided in Section 3. In the last section, some examples assessing the feasibility of the method and illustrating its great potential are presented.

2 Digital Image Correlation (DIC)

The DIC framework used in the following is detailed in this section in a similar way as in [7]. This formalism is generic that convenient for the development presented in the next section. Also, it allows for analyzing the noise sensitivity behaviour of the method that is of primary importance in an experimental context.

2.1 Formulation

From two grey level images f and g of a given sample, DIC consists in a nonlinear minimization process that identifies the displacement field $\boldsymbol{u}$ that produces the advection of the local texture:

$$\boldsymbol{u} = \text{Arg Min} \sum_{p \in ROI} [f(\mathbf{x_p}) - g(\mathbf{x_p} + \mathbf{u}(\mathbf{x_p}))]^2, \tag{1}$$

where p is the index of a pixel within the Region Of Interest (ROI) over which the computation is performed and $\mathbf{x_p}$ the co-ordinates of pixel p on the image frame. For solving this minimization problem two main routes can be distinguished. A non-parametric route is proposed in [3]. In this approach, no assumption is made on the variation of the displacement and the problem is solved pixel-wise using a staggered algorithm with relaxation and smoothing steps. The second route consists in a parametrization of the displacement as follows

$$\boldsymbol{u}(\mathbf{x}) = \sum_{k \in \mathcal{N}} u_k \boldsymbol{N}_k(\mathbf{x}). \tag{2}$$

In this decomposition, $\mathcal{N}$ is the set of degrees of freedom (DOFs) u_k, and $\boldsymbol{N}_k$ are the shape functions. Different parametrization can be used. The particular case of crack tip fields required the use of Williams' series as basis functions [10]. Other specific bases, like for 4-point bending test [11] or Brazilian test [12] can be used but for arbitrary displacement, finite element based [4, 13] or CAD based kinematics [14, 15] are more appropriate.

From a first guess for the displacement, an iterative prodecure is run until convergence is reached. Assuming that the solution increment $\mathrm{d}\mathbf{u}$ is small enough, a first order Taylor expansion of $g(\mathbf{x_p} + \mathbf{u}(\mathbf{x_p}) + \mathrm{d}\mathbf{u}(\mathbf{x_p}))$ is used to linearized the functional. After some manipulations, we obtain that the solution increment is calculated through:

$$[\tilde{\mathbf{M}}_{DIC}]\ \{\mathrm{d}\mathbf{U}\} = \{\tilde{\mathbf{b}}_{DIC}\}, \tag{3}$$

with

$$[\tilde{\mathbf{M}}_{DIC}] = [\mathbf{N}]^T[\nabla\mathbf{G}][\nabla\mathbf{G}][\mathbf{N}], \tag{4}$$

and

$$\{\tilde{\mathbf{b}}_{DIC}\} = [\mathbf{N}]^T[\nabla\mathbf{G}]\{\mathbf{F} - \mathbf{G}\}, \tag{5}$$

∇ denoting spatial derivation. $[\mathbf{N}]$ is a matrix that collects the value of the basis functions at the pixels, $[\nabla\mathbf{G}]$ a diagonal matrix that collects the values of $\nabla g(\mathbf{x_p} + \mathbf{u}(\mathbf{x_p}))$ and $\{\mathbf{F} - \mathbf{G}\}$ a vector containing the values of $f(\mathbf{x_p}) - g(\mathbf{x_p} + \mathbf{u}(\mathbf{x_p}))$. For the sake of clarity, indices indicating the iteration number have been omitted. For a detailed description of the algorithm in a multiscale framework, and its implementation the interested reader may refer to Réthoré *et al.* [16]. To reduce computational cost, a modified algorithm is adopted: we substitute $\nabla\mathbf{G}$, which depends on the current solution vector, by $\nabla\mathbf{F}$. The modified system to solve thus becomes

$$[\mathbf{M}_{DIC}]\ \{\mathrm{d}\mathbf{U}\} = \{\mathbf{b}_{DIC}\}, \tag{6}$$

with

$$[\mathbf{M}_{DIC}] = [\mathbf{N}]^T[\nabla\mathbf{F}][\nabla\mathbf{F}][\mathbf{N}], \tag{7}$$

and

$$\{\mathbf{b}_{DIC}\} = [\mathbf{N}]^T[\nabla\mathbf{F}]\{\mathbf{F}-\mathbf{G}\}. \tag{8}$$

The advantage of such a modification is that $\mathbf{M}_{DIC}$ and parts of $\mathbf{b}_{DIC}$ can be computed once for all. Note that when convergence is reached, $\nabla\mathbf{F}$ equals $\nabla\mathbf{G}$. After a few iterations (2 or 3), the modified algorithm and the initial one reveal close to identical.

2.2 Noise sensitivity

Following Réthoré *et al.* [17], we can derive the correlation kernel of the noise affecting the displacement due to a spatially uncorrelated image noise. Instead of considering that both reference and deformed images are affected by noise (of standard deviation σ), it is more convenient to report the noise on the deformed image only and to increase its amplitude by a factor 2. We have

$$\langle\{\delta\mathbf{G}\}\rangle = 0 \qquad \langle\{\delta\mathbf{G}\}\{\delta\mathbf{G}\}^T\rangle = 2[\mathbf{I}]\sigma^2 \tag{9}$$

where $\delta\mathbf{G}$ is the vector collecting the values of the realizations of the deformed image noise, $\langle\bullet\rangle$ is the average operator over the realizations of $\bullet$, σ is the standard deviation of the image noise and $\mathbf{I}$ the identity matrix which dimension is the number of pixels in the ROI. In Equation (6), only $\mathbf{G}$ is noisy. The displacement perturbation thus writes

$$\{\delta\mathbf{U}\} = [\mathbf{M}_{DIC}]^{-1}[\mathbf{N}]^T[\nabla\mathbf{F}]\{\delta\mathbf{G}\}. \tag{10}$$

From this equation, we obtain that the displacement perturbation $\boldsymbol{\delta U}$ has no systematic bias

$$\langle\{\delta\mathbf{U}\}\rangle = 0 \tag{11}$$

and that its covariance matrix is written as follows:

$$\langle\{\delta\mathbf{U}\}\{\delta\mathbf{U}\}^T\rangle = 2[\mathbf{M}_{DIC}]^{-1}[\mathbf{M}_{DIC}][\mathbf{M}_{DIC}]^{-1}\sigma^2 = 2[\mathbf{M}_{DIC}]^{-1}\sigma^2. \tag{12}$$

The noise affecting the displacement is thus not a white noise. Its correlation kernel is given by $[\mathbf{M}_{DIC}]^{-1}$. The displacement noise is not uniform and depends on the texture of the image around each nodes of the finite element mesh. $[\mathbf{M}_{DIC}]^{-1}$ is not diagonal the perturbation affecting the displacement has a spatial correlation that is a signature of the parametrization introduced in Equation (2)) noise. In practice, $[\mathbf{M}_{DIC}]^{-1}$ can be seen as a confidence indicator on the estimation of each DOF.

2.3 Condensation

At this point, it is interesting to draw the attention on the following assessment: for any parametrization of the displacement field through $\boldsymbol{N}_k$ shape functions, DIC allows for estimating directly from the images the corresponding DOFs u_k. If Williams' series are used as in [10], a direct access to stress intensity factors is provided. An other interesting example is described in [6, 7]: the finite element displacement is considered as depending on the parameters of the constitutive law of the material. The DIC problem is then solved using not the full finite element parametrization but a combination of the finite element shape functions corresponding to the sensitivity of the displacement fields to the material parameters. In this context DIC provides for a measurement of the material parameters.

A general condensation method is proposed from a finite element parametrization of the displacement. In this case, $\boldsymbol{N}_k$ are finite element shape functions and u_k nodal displacements. Let us consider that the meaningful quantities arenot the nodal displacement but linear combination of them. A linear condensation operator $\mathbf{L}$ from which the nodal displacement $\mathbf{L}$ are derived according to

$$\{\mathbf{U}\} = [\mathbf{L}]\ \{\boldsymbol{\Lambda}\}. \tag{13}$$

In this formalism, $\mathbf{\Lambda}$ collects the value of the generalized DOFs corresponding to the amplitude of the linear combination of nodal displacements defined by $\mathbf{L}$. The DIC problem can be solved using this condensation with the following system

$$[\mathbf{M}_{MIC}]\ \{\mathrm{d}\mathbf{\Lambda}\} = \{\mathbf{b}_{MIC}\}, \tag{14}$$

with

$$[\mathbf{M}_{MIC}] = [\mathbf{L}]^T\ [\mathbf{M}_{DIC}][\mathbf{L}], \quad \{\mathbf{b}_{MIC}\} = [\mathbf{L}]^T\{\mathbf{b}_{DIC}\}. \tag{15}$$

And the noise sensitivity analysis leads to the result below:

$$\langle\{\delta\mathbf{\Lambda}\}\{\delta\mathbf{\Lambda}\}^T\rangle = 2\ [\mathbf{M}_{MIC}]^{-1}\ \sigma^2 = 2\ [[\mathbf{L}]^T\mathbf{M}_{DIC}[\mathbf{L}]]^{-1}\ \sigma^2. \tag{16}$$

The sensitivity of the generalized DOFs $\mathbf{\Lambda}$ holds not only the signature of the image texture and the finite element shape functions but also the spatial correlation introduced by $\mathbf{L}$. Note that, as for the initial formulation, the average over the realizations of the perturbation induced on $\mathbf{\Lambda}$ vanishes.

3 Mechanical Image Correlation (MIC)

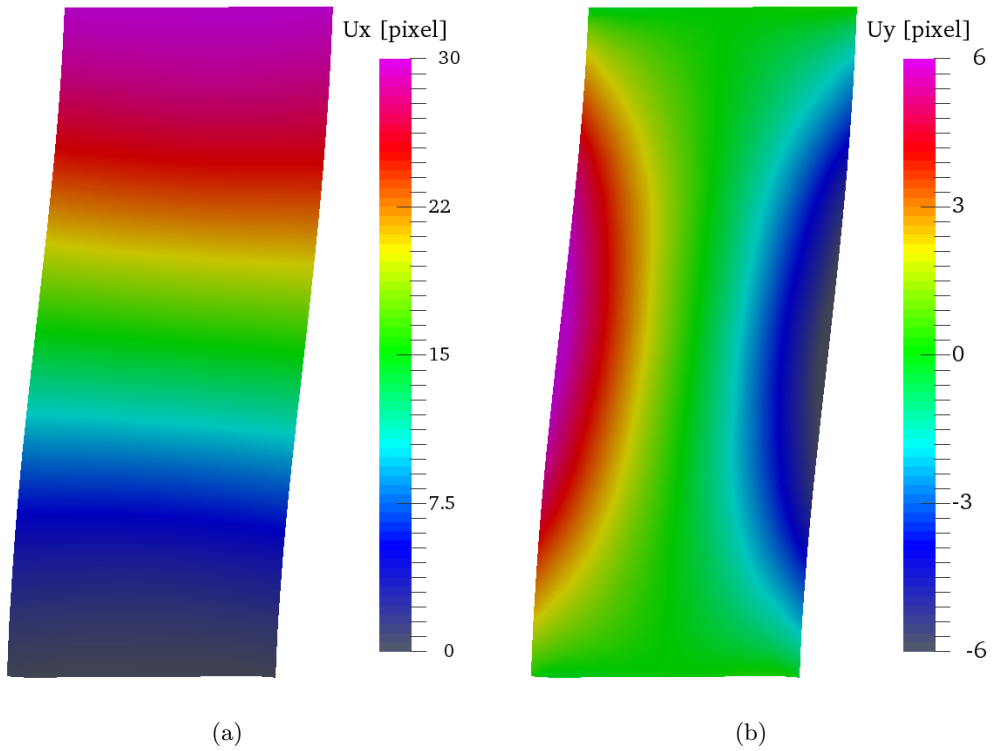

Figure 1: Horizontal and vertical displacement (in pixel) by MIC analysis for the linear isotropic test case.

The approaches in [6, 7], are parametric identification techniques: they allow for estimating experimentally from heterogeneous stress/strain states the parameters of a constitutive law from digital images and load measurements. These methods give access to a stress field compatible with the presumed constitutive law. As evidenced in the introduction, this is limiting in those cases when explicitly writing the constitutive equations is not possible. The purpose of this section is to propose a parametrization of the displacement field that derives from the local stress field with no *a priori* assumption on the constitutive law. Then using the condensation method proposed in Section 2.3, the local stress field is accessed as generalized DOFs.

Let $\mathcal{C}$ be an elastic operator. Then, an elastic solution $\mathbf{u}_o, \boldsymbol{\sigma}_o$ according to $\mathcal{C}$ and balancing the measured load F_o is computed using a standard finite element solver. The vector collecting the nodal

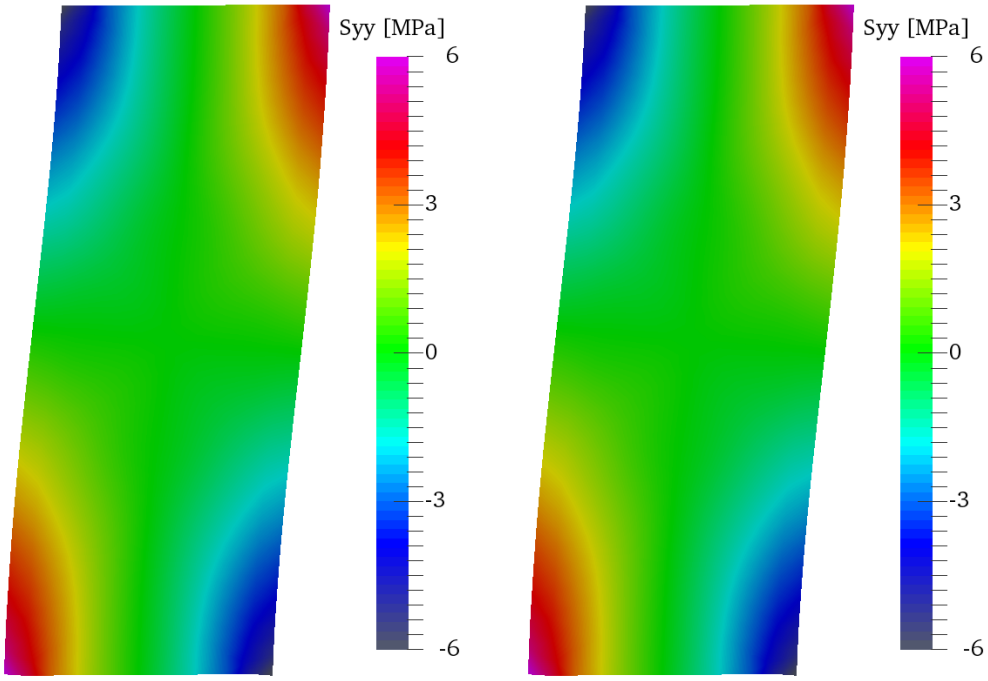

(a) (b)

Figure 2: Vertical stress field (in MPa) for the linear isotropic test case: (a) FE simulation used to generate the synthetic image, (b) MIC analysis.

displacement of this elementary solution is denoted by $\mathbf{U}_o$. Without loss of generality, the actual displacement is written as

$$\mathbf{u} = \mathbf{u}_o + \bar{\mathbf{u}}. \tag{17}$$

$\bar{\mathbf{u}}$ results from the gap between the actual constitutive behaviour of the material (locally) and elasticity according to $\mathcal{C}$. As $\mathbf{u}_o, \boldsymbol{\sigma}_o$, balances the external load F_o, then it is concluded that the stress field $\bar{\boldsymbol{\sigma}}$, which is the gap between the actual stress field $\boldsymbol{\sigma}$ and $\boldsymbol{\sigma}_o$, from which $\bar{\mathbf{u}}$ derives, is a self-balanced stress field. It has the following properties:

$$\text{div}\bar{\boldsymbol{\sigma}} = 0 \text{ over the ROI} \quad \bar{\boldsymbol{\sigma}}\mathbf{n} = 0 \text{ over the boundary of ROI} \tag{18}$$

Using $\mathcal{C}$, an elastic strain $\bar{\varepsilon}_e$ is obtained from $\bar{\boldsymbol{\sigma}}$. This strain may not fulfill the strain compatibility equation in general and the actual strain $\bar{\varepsilon}$ derived from $\bar{\mathbf{u}}$ is thus written as

$$\bar{\varepsilon} = \bar{\varepsilon}_e + \bar{\varepsilon}_a, \tag{19}$$

where $\bar{\varepsilon}_a$ is a anelastic strain field accommodating strain compatibility constraint. Within this context, $\bar{\mathbf{u}}$ is a function of a self-balanced stress field $\bar{\boldsymbol{\sigma}}$ and an anelastic strain field $\bar{\varepsilon}_a$. If Equation 18 rewritten using Equation 19, one obtains:

$$\text{div}(\mathcal{C}\bar{\varepsilon}) - \text{div}(\mathcal{C}\bar{\varepsilon}_a) = 0 \text{ over the ROI} \quad (\mathcal{C}(\bar{\varepsilon} - \bar{\varepsilon}_a))\mathbf{n} = 0 \text{ over the boundary of ROI} \tag{20}$$

This is a similar problem ones has to solve for thermo-elasticity, or for elasticity with volume forces. If $\bar{\varepsilon}_a$ is given then $\bar{\mathbf{u}}$ is the solution of a linear elastic problem. There exists three kinds of $\bar{\varepsilon}_a$ fields:

I the associated elastic stress field $\mathcal{C}\bar{\varepsilon}_a$ is self-balanced. In this case the volume forces in Equation 20 vanish and because the computation of $\bar{\mathbf{u}}$ relies on an elastic problem, the trivial solution $\bar{\mathbf{u}} = \mathbf{0}$ is obtained.

II $\mathcal{C}\bar{\varepsilon}_a$ is not self-balanced but $\bar{\varepsilon}_a$ is compatible, *i.e.* there exists a displacement $\bar{\mathbf{u}}_a$ such that $\bar{\varepsilon}_a$ is its symmetric gradient ($\bar{\varepsilon}_a = \nabla^S \bar{\mathbf{u}}_a$). In this case $\bar{\varepsilon} = \bar{\varepsilon}_a$ and thus $\bar{\varepsilon}_e = 0$. This means that $\bar{\boldsymbol{\sigma}}$ vanishes and $\bar{\mathbf{u}} = \bar{\mathbf{u}}_a$ derives from a compatible strain field.

III $\mathcal{C}\bar{\varepsilon}_a$ is neither self-balanced nor compatible. In this case $\bar{\varepsilon}$ is different from $\bar{\varepsilon}_a$ and $\bar{\boldsymbol{\sigma}}$ does not vanish.

Type I fields has no effect on $\bar{\mathbf{u}}$. But type II and III produce an additional displacement for which one has to propose a parametrization. This is the purpose of the next two paragraphs.

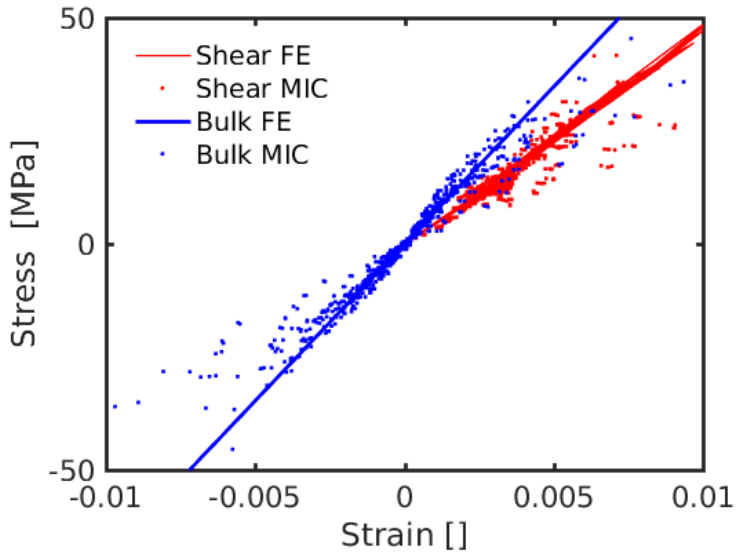

Figure 3: Stress *v.s.* strain spherical and deviatoric components: comparison between FE simulation and MIC measurement.

3.1 Type II anelastic fields

Type II anelastic fields are such that $\mathcal{C}\bar{\varepsilon}_a$ is not self balanced but $\bar{\varepsilon}_a$ is compatible. As a consequence, $\bar{\mathbf{u}}$ is solution of an elasticity problem with volume forces deriving from a compatible strain field and $\bar{\varepsilon}_a = \bar{\varepsilon}$. Numerically, it is convenient to generate a set of elastic solution for this problem from the eigen modes of the elastic finite element stiffness matrix. This set of eigen modes is stored in matrix format as $\mathbf{U}_{II}$. In this case the set of anelastic fields is $\mathbf{E}_{aII}$ that is the symmetric gradient of $\mathbf{U}_{II}$ components.

3.2 Type III anelastic fields

For type III fields, $\mathcal{C}\bar{\varepsilon}_a$ is neither self-balanced nor compatible. In this case $\bar{\mathbf{u}}$ is solution of an elasticity problem under volume forces. Let $\mathbf{E}_a$ be a basis for anelastic strain. It has the same dimensionality as a basis for symmetric tensor fields as their is no compatibility constraints to fulfill at this point. Using this set of anelastic strain field, internal finite element force vectors $\mathbf{F}_{int}$ are assembled. Then, a singular value decomposition is performed to extract from the anelastic strain field basis those generating volume forces (those that are not of type I). From this selection of internal force vectors, a set of anelastic fields $\mathbf{E}_{aIII}$ and corresponding elastic solution $\mathbf{U}_{III}$ balancing the corresponding volume forces are derived.

3.3 Displacement parametrization

Based on the construction of these bases, the parametrization of the displacement $\mathbf{u}$ is achieved. The first component of this parametrization is $\mathbf{U}_o$. This displacement vector is obtained from a FE elastic simulation using $\mathcal{C}$ as the elastic tensor and a prescribed displacement measured by DIC along the boundary of the ROI where non-zero stress conditions apply. The amplitude of this displacement is adjusted so that the resulting forces F_o matched the experimental data. Note that because $\mathcal{C}$ may not be the actual constitutive operator, after adjustment of F_o, the displacement along the boundary of the ROI does not match the measured displacement anymore.

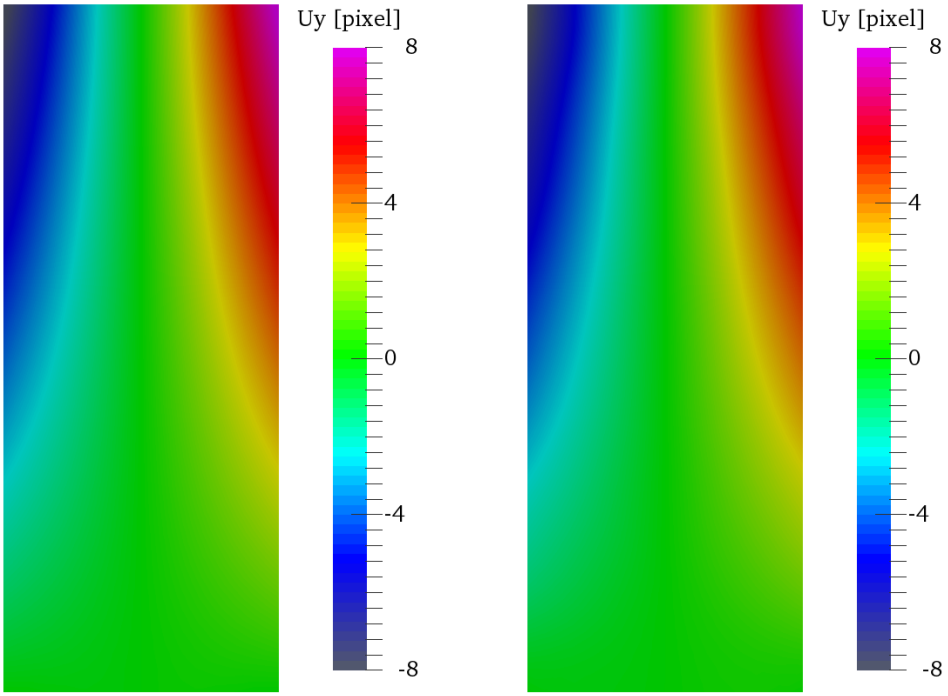

(a) (b)

Figure 4: Comparison of the horizontal displacement (in pixel) from the FE simulation (a) and measured by MIC for the test case with residual stress.

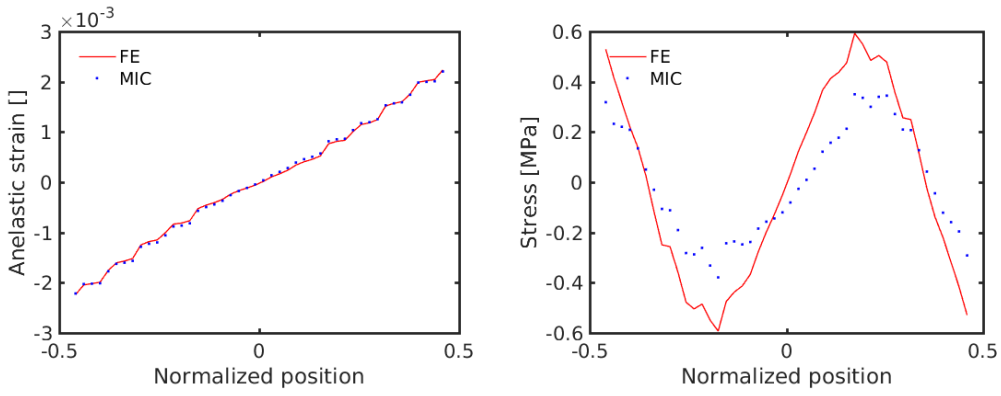

(a) (b)

Figure 5: Comparison of yy component of the anelastic strain (a) and residual stress (b) from the FE simulation and measured by MIC for the test case with residual stress.

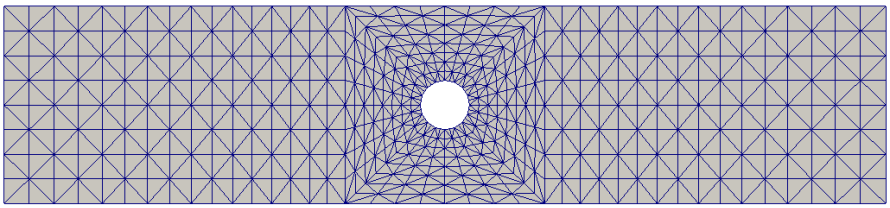

(a)

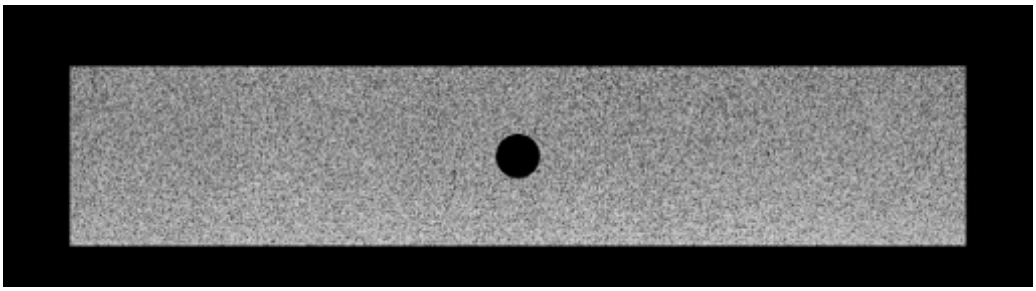

(b)

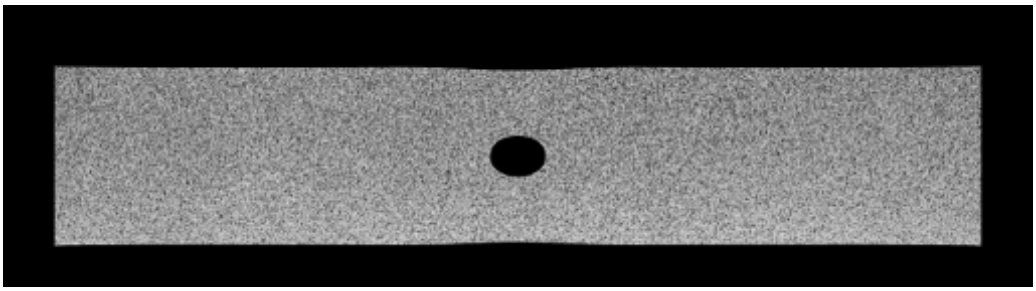

(c)

Figure 6: Finite element mesh for the MIC analysis. Initial and last images generated from the FE simulation.

The next terms of the displacement parametrization are obtained from the anelastic fields namely, $\mathbf{U}_{II}$ and $\mathbf{U}_{III}$. This parametrization does not contain rigid body motions (two translations and one rotation in 2D) that are considered through additional basis vectors $[\mathbf{U}_R]$. These two bases are then concatenated as $[\bar{\mathbf{U}}] = [\mathbf{U}_{II}\mathbf{U}_{III}\mathbf{U}_R]$ for describing $\bar{\mathbf{u}}$.

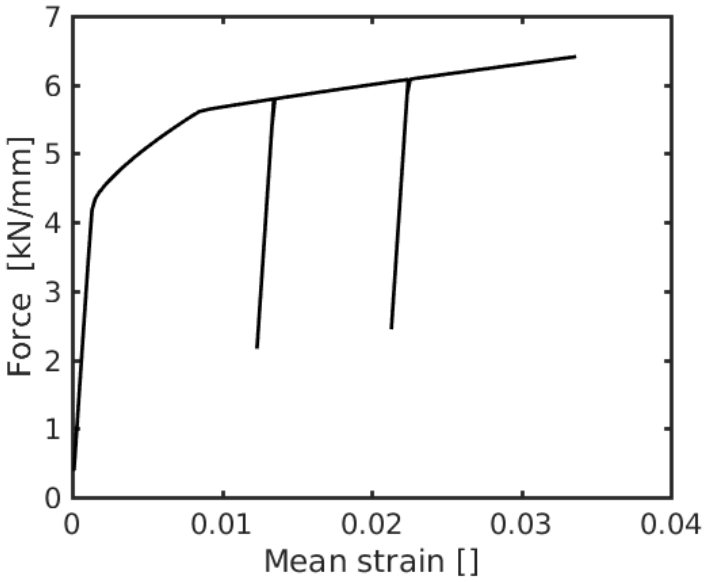

Figure 7: Global loading history for the FE simulation.

3.4 Resolution

A parametrization of the displacement is proposed above. The amplitude of one of the basis functions is known *a priori* to ensures that the external force resulting from the measured stress matches the measured force. The deformed image g is thus advected by $\mathbf{u}_o + \bar{\mathbf{u}}$ and the DIC problem solved with respect to the parameter involved in the parametrization $[\bar{\mathbf{U}}]$ only. Following Section 2.3, The DIC problem is solved with a condensation operator $\mathbf{L}$ equal to $\bar{\mathbf{U}}$. The DIC problem is then solved following Section 2.3.

Using the proposed methodology, DIC provides for the amplitude of $[\bar{\mathbf{U}}]$ components, let us say $\bar{\Lambda}$. This of course give a direct access to the measured displacement and total strain field. In a post-processing step, anelastic strain field $\bar{\varepsilon}_a$ is derived from $\mathbf{E}_{aII}$, $\mathbf{E}_{aIII}$ and the corresponding components of $\bar{\Lambda}$. The stress field is then reconstructed from $\boldsymbol{\sigma}_o$ derived from $\mathbf{u}_o$ and $\bar{\boldsymbol{\sigma}}$ that is derived from the additional elastic strain $\bar{\varepsilon}_e = \bar{\varepsilon} - \bar{\varepsilon}_a$.

Note that the decomposition adopted herein is completely generic as no assumption is made on the form of the constitutive relation. The only assumption is on the anelastic field that measures the distance to linear elasticity according to a given but arbitrary elastic tensor $\mathcal{C}$. Changing the value of $\mathcal{C}$ changes the estimation of $\bar{\varepsilon}_a$ but not that of $\boldsymbol{\sigma}$. Depending on the type of constitutive laws, different interpretations hold for $\bar{\varepsilon}_a$. For example, if $\mathcal{C}$ is the actual elastic tensor and the material is elasto-plastic then $\bar{\varepsilon}_a$ is the plastic strain. If a damage law is expected, then $\bar{\varepsilon}_a$ provides for a direct access to material degradation.

4 Examples

To illustrate the capability of the proposed method to measure stress, strain and anelastic strain fields from digital images, synthetic data are generated. A finite element simulation is run and the result from this simulation is used to generate a set of deformed image given a reference speckle pattern. Three test cases are provided. The first one is aimed at retrieving material parameters for linear isotropic elasticity. The relevance of MIC measurement relies in this case on the activation of type

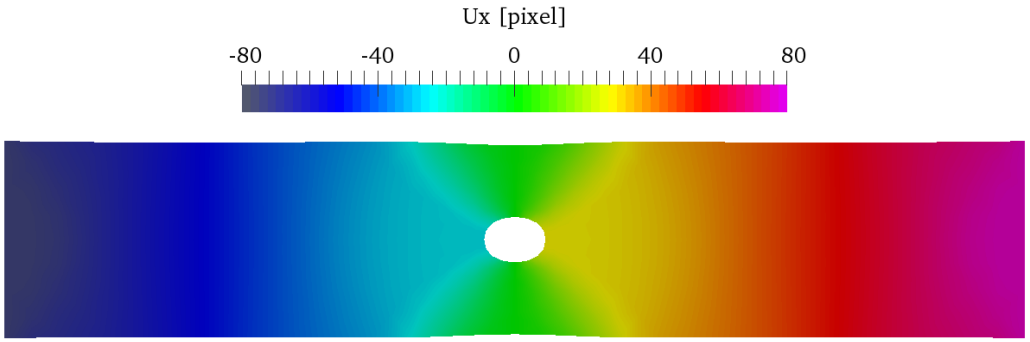

(a)

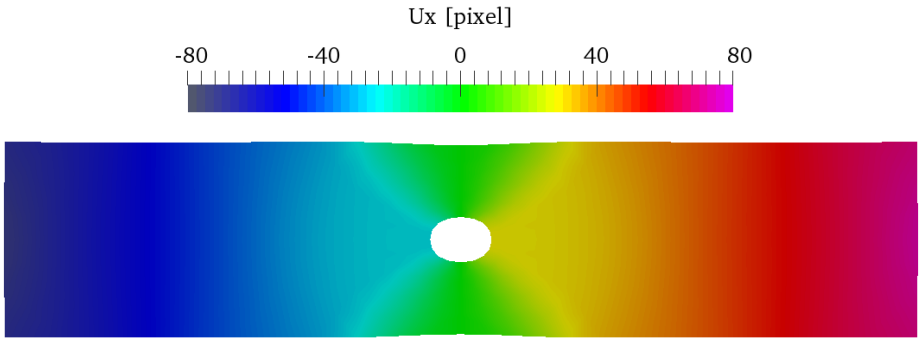

(b)

Figure 8: Displacement (in pixel) in the loading direction at the last step for (a) a DIC analysis and (b) a MIC analysis.

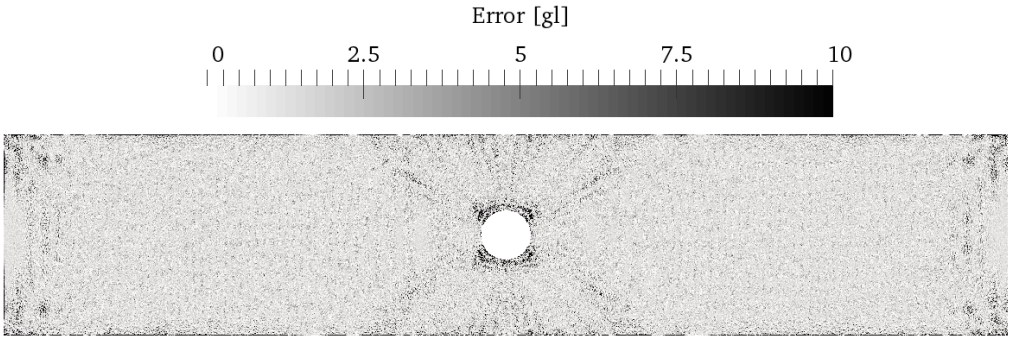

(a)

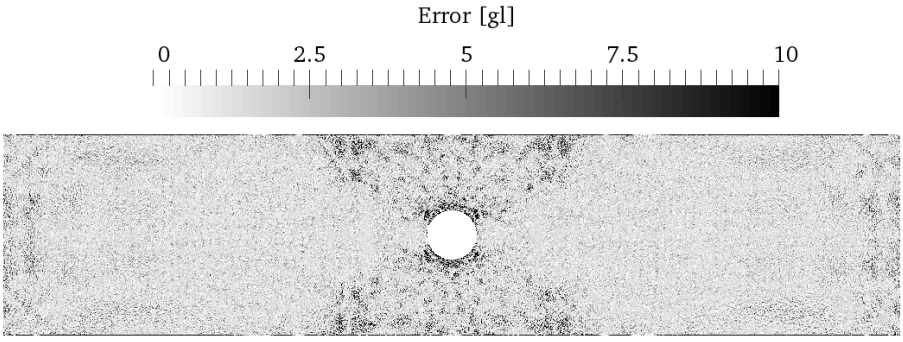

(b)

Figure 9: Correlation error map in grey level at the last step for (a) a DIC analysis and (b) a MIC analysis.

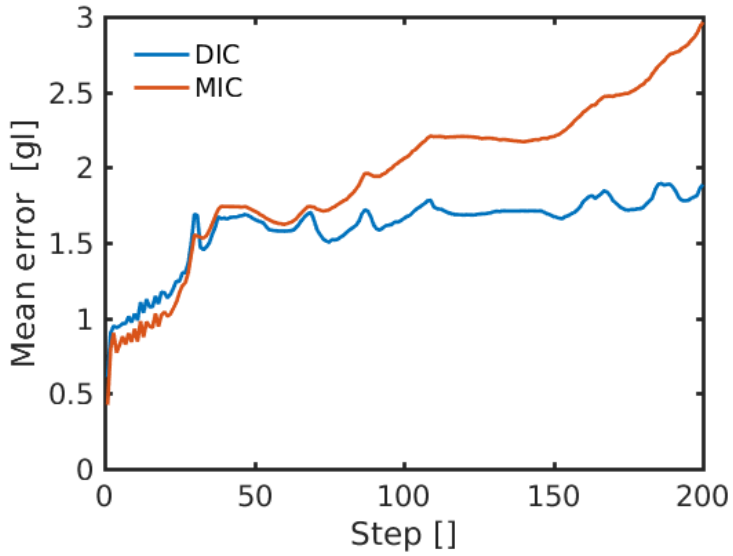

Figure 10: Comparison of the average correlation error in grey level for the DIC and MIC analysis.

II anelastic fields. The second one is dedicated to the evaluation of residual stress (relying on the activation of type III anelastic strain fields) and the third one deals with elasto-plasticity (relying of both type II and III anelastic strain fields).

4.1 Isotropic linear elasticity

In this example, the model consists in a rectangular domain of 1400×3500 pixels. In the FE simulation used for generating the synthetic data, the displacement along the bottom edge is clamped while along the top edge, the vertical displacement is set to 0 but the horizontal displacement is prescribed to 30 pixels. In this numerical simulation the material is assigned a linear isotropic behaviour defined by its Young's modulus and Poisson's set to 5 GPa and 0.2 respectively.

For the MIC analysis, these material parameters are changed so that $\mathcal{C}$ differs from the actual elastic tensor. They are set to 2.5 GPa and 0.1 respectively. A mesh of triangular elements of 96-pixel size is used and 100 modes are used for each anelastic strain field bases. The displacement field obtained from this analysis are depicted in Figure 1. They are almost identical to the displacement obtained by DIC and that used to generate the deformed image. To assess the accuracy of the stress field measurement, the measured stress component in the vertical direction is compared to its homologous field in the numerical simulation in Figure 2. It is worth noting that there is a very good agreement between the measurement and the actual values of stress. To further demonstrate how the actual constitutive law is retrieved from the MIC analysis, the spherical and deviatoric parts of the stress tensor are plotted against their strain counterpart in Figure 3. It is obtained that a linear regression in the cloud of material state points obtained by MIC would allow for retrieving the actual elastic constants.

4.2 Residual stress

In this example, the same geometry as in the previous one is considered. The material is assigned the same properties. The FE simulation is run to simulate the existence of a remaining elasto-plastic strain field. To make this remaining strain not compatible, only its yy component is considered and a linear evolution along x from -0.0025 to 0.0025 is assigned. An elastic problem is solved under the volume forces generated by this residual strain and the deformed image is generated by using the resulting displacement field. In Figure 4, the measured and prescribed displacement are compared. A good agreement is obtained. This is confirmed in Figure 5 which compares prescribed and measured of vertical anelastic strain and stress respectively. For plotting these curves, the element wise values of the fields have been re-interpolated on a regular grid and then averaged along the y direction. The

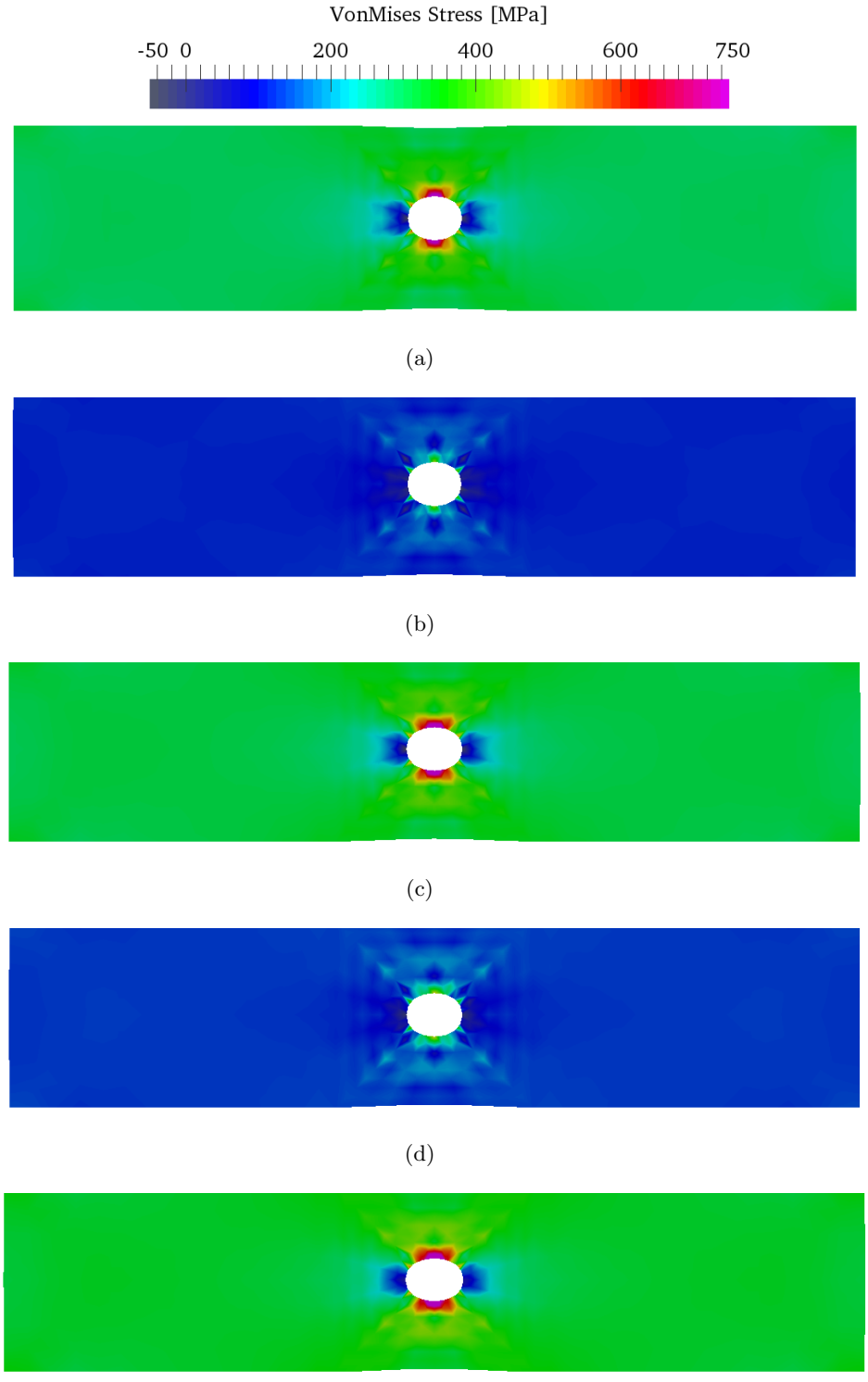

Figure 11: Evolution of the stress component in the axial direction in MPa: (a) just before the first unloading, (b) at the first unloading, (c) just before the second unloading, (d) at the second unloading and (e) at the last step.

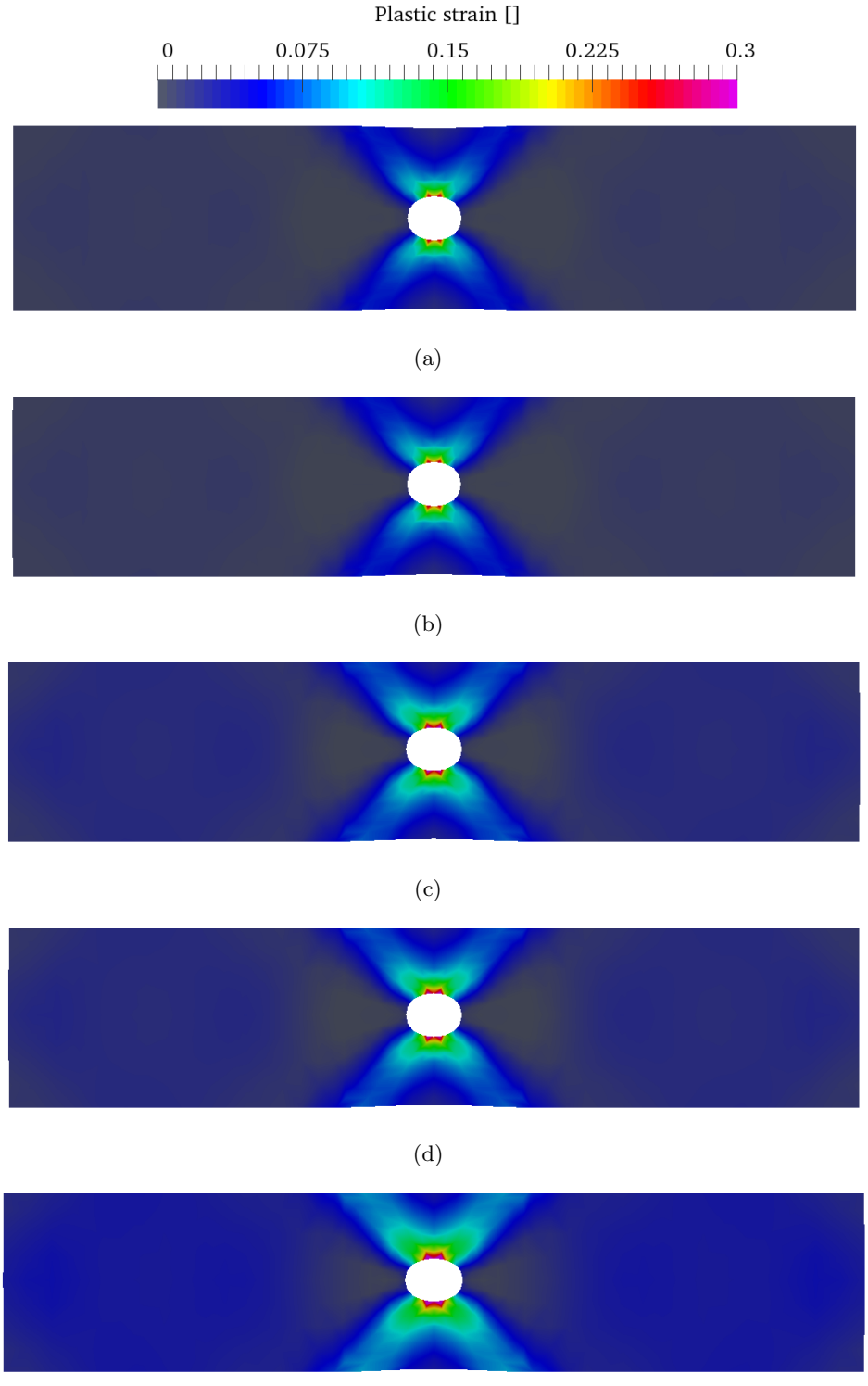

Figure 12: Evolution of the anelastic strain norm: (a) just before the first unloading, (b) at the first unloading, (c) just before the second unloading, (d) at the second unloading and (e) at the last step.

residual strain distribution is retrieved almost perfectly by MIC. The residual stress measurement is slightly less accurate but one has to point out that this residual stress level derive from elastic strain lower than 0.0001 (far below the usual resolution of DIC).

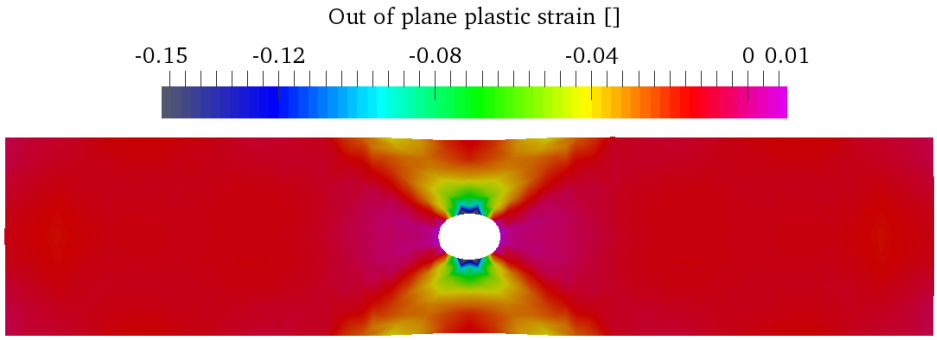

Figure 13: Out of plane component of the plastic strain at the last step.

4.3 Elasto-plasticity

A rectangular sample of $100 \times 20\text{mm}^2$ with a hole of diameter 5 mm is considered. It is assigned an elasto-plastic behaviour with linear isotropic hardening. The Young's modulus is 168 GPa, the initial yield stress 284 MPa and the hardening coefficient 1.48 GPa. The Poisson's ratio is 0.25. The numerical simulation is run with a mesh similar to that shown in Figure 6(a) but with one additional subdivision. A 2D plane stress formulaton is used. The reference image is depicted in Figure 6(b) and last deformed image in Figure 6(c). The size of the images is 5120×1400 pixels, corresponding to a physical pixel size of 22.2 μm. The speckle pattern for the initial image is a real one taken from an image of a real sample. The load history applied in the simulation is illustrated in Figure 7. 200 steps are performed. Two unloading stages are considered at step 40 and 120.

The MIC analysis is run using 500 type II modes and 300 type III modes. The elastic tensor $\mathcal{C}$ is assigned the same value as the elastic tensor for the numerical simulation used to generate the images. In the DIC analysis, the displacement estimation along the boundary of the finite element mesh are usually less robust than in the bulk. To avoid that this lower robustness affects the result of the MIC analysis where the DIC displacement is used as boundary conditions for computing the admissible elastic solution $\mathbf{u}_o$, one layer of elements is removed at both ends of the mesh. The DIC displacement used as boundary conditions is thus picked up from nodes in the bulk of the DIC mesh. The displacement fields measured by DIC and MIC using the mesh in Figure 6(a) for the last image are depicted in Figure 8. The scatter between the two displacements is difficult to observe by the naked eyes. For assessing the accuracy of the displacement field obtained by MIC, the correlation error map are plotted for the two analyses in Figure 9. This two error maps are again difficult to distinguish what confirms that the MIC displacement leads to a registration of the images of the same accuracy as the DIC analysis. To further assess this point, the average correlation error for DIC and MIC is plotted as a function of the steps in Figure 10. These results ensure that the displacement parametrization adopted for MIC leads to measured fields as accurate as thoses obtained for a DIC analysis.

MIC also provides for the estimation of meaningful mechanical fields. First the evoluton of the stress component in the loading direction is provided in Figure 11. The decrease of the stress during unloading is well captured as well as its progressive increase during the loading stages. Concerning the anelastic strain $\bar{\varepsilon}_a$, it is plotted in Figure 12. In Figure 12, the norm of the anelastic strain is plotted for the same step as the stress in Figure 11. It is observed, as expected for an elasto-plastic material for which it corresponds to the plastic strain, that the anelastic strain is kept constant during unloading. Note that the norm of the tensor includes the contribution of the out of plane component which has been derived using plastic incompressibility. The latter is plotted for the last step in Figure 13. Expected results like shrinkage at the pole of the hole are retrieved.

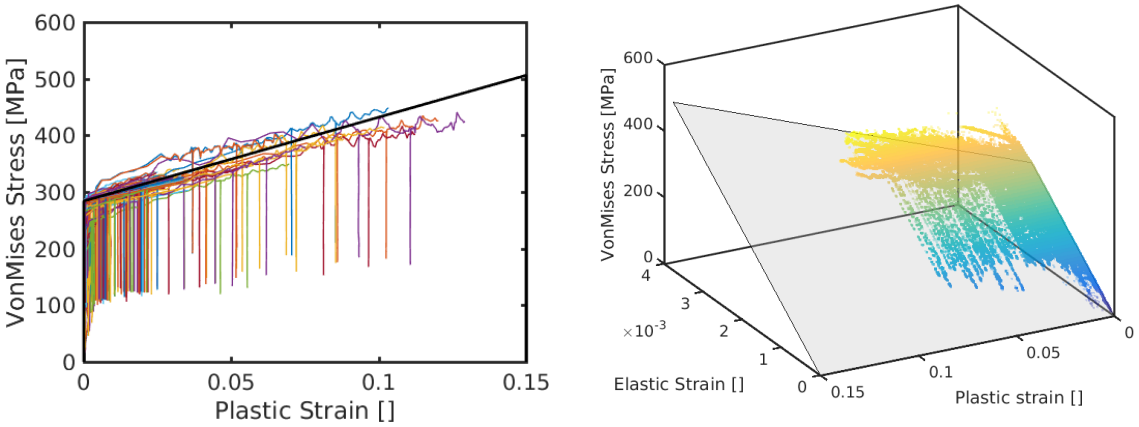

(a) (b)

Figure 14: Stress strain plots for the material state database obtained by MIC.

To further illustrate the capability of MIC to measure stress fields, an analysis of the entire set of measured material states is provided in Figure 14. This set consists in more than 600 000 point in the space defined by the components of the stress, strain and anelastic strain tensors. For visualization purposes, ones needs to reduce the dimensionality of this database. Because it is assumed that VonMises plasticity holds, the VonMises stress is computed as well as the deviatoric part of the elastic strain and the norm of the anelastic strain. In Figure 14(a), the evolution of the VonMises stress is plotted as a function of the norm of the plastic strain for a few points. The typical loading unloading scenario of elasto-plasticity is captued. In Figure 14(b), VonMises stress is plotted as a function of the deviatoric part of the elastic strain and the norm of the plastic strain. The shape of the domain of admissible material states agrees well with the one considered in the numerical simulations used to generate the images.

5 Conclusion

A methodology is proposed to build a parametric description of the displacement field DIC which parameters are directly related to local stress and strain. With no assumption on the constitutive relation, the method allows for measuring displacement, strain and stress fields. Further, an anelastic strain field measuring the *distance* between the actual local constitutive behaviour and elasticity according to a given but arbitrary elastic tensor is obtained. The ability of the method to measure stress fields in different situations is illustrated. The raw data extracted from the measurement are admissible material states in a space of dimension 9 for 2D problems.

6 Acknowledgments

The support of Région Pays de la Loire and Nantes Métropole through grant Connect Talent IDS is gratefully acknowledged.

References

[1] Lucas BD, Kanade T, *et al.*. An iterative image registration technique with an application to stereo vision. *IJCAI*, vol. 81, 1981; 674–679.

[2] Sutton M, Cheng M, Peters W, Chao Y, McNeill S. Application of an optimized digital image correlation method to planar deformation analysis. *Image Vision Computing* august 1986; **4**(3):143–150.

[3] Vercauteren T, Pennec X, Perchant A, Ayache N. Diffeomorphic demons: Efficient non-parametric image registration. *NeuroImage* 2009; **45**(1):S61–S72.

[4] Besnard G, Hild F, Roux S. 'finite-element' displacement fields analysis from digital images: Application to portevin-le châtelier bands. *Experimental Mechanics* 2006; **46**(6):789–803.

[5] Réthoré J, Hild F, Roux S. An extended and integrated digital image correlation technique applied to the analysis of fractured samples. *European Journal of Computational Mechanics* 2009; **18**:285–306.

[6] Leclerc H, Perie J, Roux S, Hild F. *Computer Vision/Computer Graphics CollaborationTechniques*, chap. Integrated Digital Image Correlation for the Identification of Mechanical Properties. Springer: Berlin, 2009.

[7] Réthoré J. A fully integrated noise robust strategy for the identification of constitutive laws from digital images. *International Journal for Numerical Methods in Engineering* 2010; **84**:631–660, doi:10.1002/nme.2908.

[8] van der Maaten L, Postam E, van den Herik J. Dimensionality reduction: A comparative review. *Technical Report*, Tilburg, Netherlands: Tilburg Centre for Creative Computing, Tilburg University, Technical Report: 2009-005 2009.

[9] Kirchdoerfer T, Ortiz M. Data-driven computational mechanics. *Computer Methods in Applied Mechanics and Engineering* 2016; **304**:81–101.

[10] Roux S, Hild F. Stress intensity factor measurement from digital image correlation: post-processing and integrated approaches. *International Journal of Fracture* 2006; **140**(1-4):141–157.

[11] Leplay P, Réthoré J, Meille S, Baietto M. Damage law identification of a quasi brittle ceramic from a bending test using digital image correlation. *Journal of the European Ceramic Society* 2010; **30**(13):2715–2725.

[12] Hild F, Roux S. Digital image correlation: from displacement measurement to identification of elastic properties–a review. *Strain* 2006; **42**(2):69–80.

[13] Réthoré J, Hild F, Roux S. Extended digital image correlation with crack shape optimization. *International Journal for Numerical Methods in Engineering* 2008; **73**(2):248–272, doi:10.1002/nme.2070.

[14] Elguedj T, Réthoré J, Buteri A. Isogeometric analysis for strain field measurements. *Computer Methods in Applied Mechanics and Engineering* 2011; **200**(1-4):40–56.

[15] Réthoré J, Elguedj T, Simon P, Coret M. On the use of nurbs functions for displacement derivatives measurement by digital image correlation. *Experimental Mechanics* 2009; **50**(7):1099–1116, doi:10.1007/s11340-009-9304-z.

[16] Réthoré J, Hild F, Roux S. Shear-band capturing using a multiscale extended digital image correlation technique. *Computer Methods in Applied Mechanics and Engineering* 2007; **196**(49-52):5016–5030, doi:10.1016/j.cma.2007.06.019.

[17] Réthoré J, Besnard G, Vivier G, Hild F, Roux S. Experimental investigation of localized phenomena using digital image correlation. *Philosophical Magazine* 2008; **88**(28,29):3339–3355, doi:10.1080/14786430802263111.